Final Report: NRA-92-OSSA-17

Studying the Thermal/Non-Thermal Crossover in Solar Flares

R. A. Schwartz Hughes STX and Laboratory for Astronomy and Solar Physics, NASA/GSFC

Introduction:

This report describes the worked performed under contract NAS5-(32584) during the time period covered by Phase 3 of the CGRO Guest Investigator Program under NRA-92-OSSA-17 from 1 November 1993 through 1 November 1994. We have made spectral observations of the hard X-ray and gamma-ray bremsstrahlung emissions from solar flares using BATSE on CGRO. These measurements of their spectrum and time profile provided valuable information on the fundamental flare processes of energy release, particle acceleration, and energy transport. Our scientific objective was to study both the thermal and non-thermal sources of solar flare hard x-ray and gamma-ray emission. Thesescientific objectives were met through two mutually supporting tasks:

1. Create and refine tools for spectroscopic and time series analysis for all BATSE solar investigators official and unofficial and to provide easy access into an on-line database of BATSE flare events.

2. Participate in the effort to inter-calibrate the BATSE detectors with the current generation of spaceborne hard x-ray and gamma-ray instrumentation in order to maximize the yield of the spectroscopic analysis.

Work Performed:

Work was performed in several different areas in support of the contract:

Refined IDL procedures for the data reduction of BATSE data types in both FITS and BATSE native format. These procedures have been integrated into an overall analysis package which has been made available to the BATSE solar guest investigator community. The package, called SPEX, is now used worldwide via the Internet and supports the display of time histories and energy spectra as well as the complete analysis of data from instrumental units to physical quantities at the emission site. Much work has been done to refine the SPEX package including extensive development of a graphical-user-interface to the program. Currently there are 6-10 users of this analysis code. The user interface is shown in Figure 1.

Continuing the collaborative analysis of the 30 June 1991 solar flare with fellow BATSE guest investigator, Dr. Nicole Vilmer, of the Paris Observatory at Meudon. The BATSE data from the LADs and the SPECs have been converted to photon spectra for comparison with gamma-ray observations obtained with the Phebus spectrometer on the GRANAT spacecraft. We also compared the gamma-ray spectrum obtained with BATSE with the time-resolved spectra from EGRET on CGRO.

Collaborated with Markus Aschwanden to analyze hard X-ray time structures using the complete set of 64 msec BATSE data. We have found that there is a 16 msec delay of the lowest energy channel (25-50 keV) when compared to the 50-100 keV channel. In a paper in review by Ap. J., (Aschwanden, Schwartz, and Alt) these

delays are interpreted as some of the first evidence of electron time-of-flight in flaring loops. See attached paper.

Have analyzed the response matrix generating algorithms for the BATSE SPEC detectors and found a significant difficulty below 40 keV. I have developed algorithms to correct this problem and am implementing it within my software. These corrections will be shared with the entire BATSE team.

Summary

We have developed analysis techniques for the reduction of the BATSE hard X-ray data from both the LADs and the SPECs resulting in the physical analysis of many solar flares. Several more works are in progress as the analysis tools are being refined and made available to more of the international solar physics community.

Figure 1.

Graphical-User-Interface to SPEX analysis code. Top row of buttons in the lower right hand panel are pull down menus giving
the user complete control over time-resolved X-ray analysis.

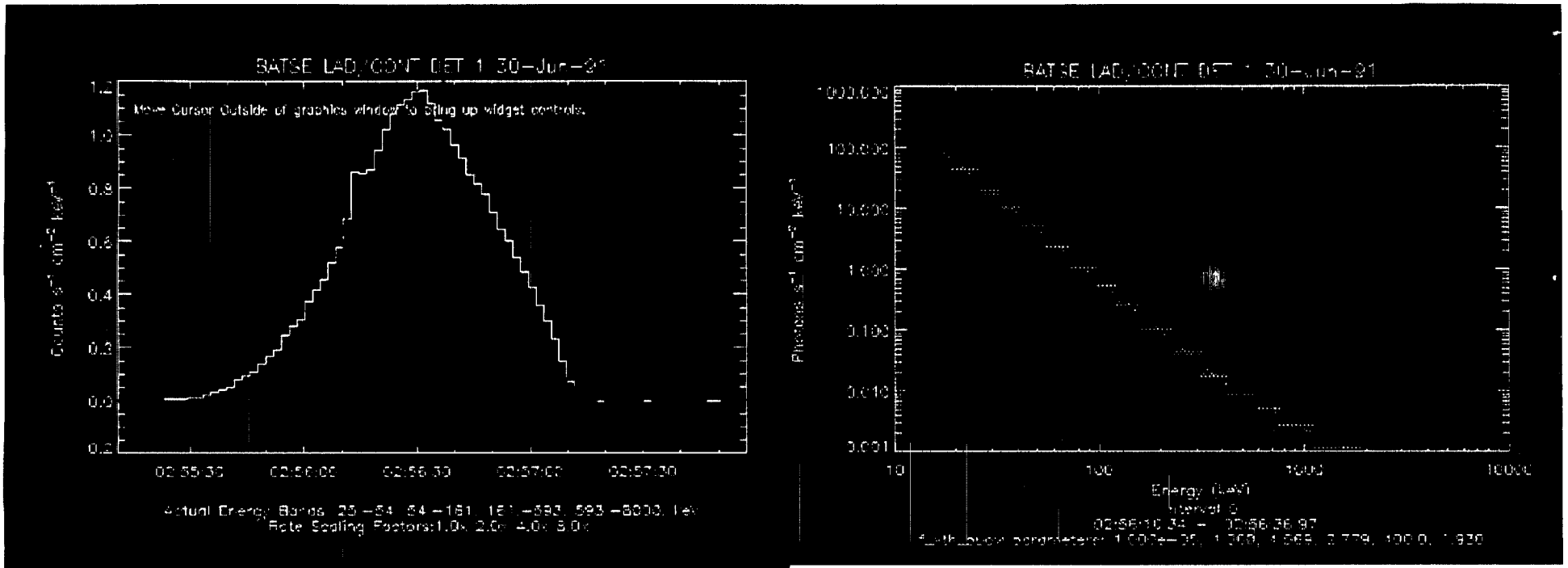

SPEX INFORMATION BOX

```
Commands from /tmp
I
  Spectral Plot and Fit Parameters:

   F_MODEL       f_vth_bpow
   APAR          1.00000e-05 1.00000    4.56927    2.77913
                 400.000    1.93000
   FREE          0          0          1          1
                 0          0
   LNORIM        0.00000000
   FIRST         0
   LAST          0
   RANGE_LO      1.00000e-07 0.500000   1.00000e-10 1.00000
                 12.0000    1.00000
   RANGE_HI      1000.00    20.0000    1.00000e+10 12.0000
                 1000.00    12.0000
   MARKOV        25.4278    11415.8
   SUMFIT        0
   SP_XTYPE      1
   SP_YTYPE      1
   SPXRANGE      0.00000    0.00000
   SPYRANGE      0.00000    0.00000
   MODE_INFO     0
```

ACTIONS: SPECIAL | TIME HISTORY | SPECTRAL FITS | SUMMARY

OPTIONS: SPECIAL | TIME HISTORY | SPECTRAL FITS | SUMMARY

EXIT

COMMAND LINE for SPEX

SELECT ONE

HELP:

- ◇ CLEAR
- ◇ SPEX OVERVIEW
- ◇ DISPLAY SPEX COMMENTS
- ◇ HELP ON ACTIONS AND OPTIONS

Electron Time-of-Flight Differences in Solar Flares

Markus J. Aschwanden
University of Maryland, Astronomy Department, College Park, MD 20742

Richard A. Schwartz
Hughes STX & Laboratory for Astronomy and Solar Physics, Code 682, NASA/GSFC, Greenbelt, MD 20771

and

Daniel M. Alt
Case Western Reserve University, Astronomy Department, Cleveland, OH 44106

Received _____; accepted _____

Submitted to *THE ASTROPHYSICAL JOURNAL*; Version: 28 Sept 1994

ABSTRACT

In the widely accepted thick-target model for hard X-ray (HXR) emission in solar flares, electron acceleration is assumed to occur near the tops of flare loops (in coronal heights), while HXR bremsstrahlung emission is produced in the chromosphere. Under this assumption, the velocity spectrum of the accelerated electrons causes time-of-flight differences that are expected to produce a small time delay for HXR emission at low energies. Here we report on the first observational evidence of such a delay. The electron time-of-flight differences between electrons that produce 25-50 keV and 50-100 keV HXR emission is found to have a distribution with a mean of 19.4 ± 1.3 ms and a standard deviation of $\sigma_\tau = 37$ ms. This result is based on the statistics of 5430 HXR pulses detected during 640 solar flares, recorded in the *DISCSC* burst trigger mode with a time resolution of 64 ms by the *Burst and Transient Source Experiment (BATSE)* onboard the *Compton Gamma Ray Observatory (CGRO)*. From the time-of-flight differences we infer a height distribution of $H \pm \sigma_H = 8400 \pm 16,000$ km for flare loops with acceleration sites at loop tops. For the electron density in flare loops we find an upper limit of $n_e \leq 8 \cdot 10^{12}$ cm^{-3}. The relatively small time-of-flight differences correspond typically to only $\approx 3\%$ of the HXR pulse duration, and therefore, no rapid variation in the spectral slope of the observed HXR spectrum is expected.

Subject headings: Sun: Corona — Sun: Flares — Sun : X-ray radiation — Particle acceleration

1. INTRODUCTION

Time-of-flight measurements are used in laboratory experiments of particle physicists to determine the kinetic energy of particles, or in combination with momentum measurements with magnetic fields, to determine the unknown mass of an unidentified particle. In laboratories, it is straightforward to measure distances and time differences, from which the velocity can be derived. For energetic electrons in solar flares, however, the location of the accelerator is not known, while the timing and velocity of accelerated electrons can possibly be inferred from their hard X-ray (HXR) emission. In this study we attempt exactly this kinematic experiment, to determine the distance between the accelerator and the collisional target by measuring time-of-flight differences between different particle energies.

Energy-dependent delays in solar flare HXR emission have been reported and predicted in several studies, with various interpretations depending on the time scale and sign of the delay. For the case where the high-energy HXR emission lags the low-energy emission, two basic models have been proposed: the trap-plus-precipitation model (Melrose & Brown 1976; Vilmer, Kane & Trottet 1982), and the second-step acceleration model (Bai & Ramaty 1979). In the trap model, the lag of the high-energy emission occurs because the collisional time scale increases with the particle energy. This delays the escape from the trap and subsequent precipitation, and thus, the resulting thick-target HXR emission. In the second-step acceleration model, a second-stage process is invoked to accelerate suprathermal electrons to higher energies. Because both of these models cannot explain an energy delay with opposite sign, they are not relevant for the interpretation of the delay at low energies observed here.

For the case where the low-energy HXR emission lags the high-energy emission, an interpretation in terms of time-of-flight differences is an obvious candidate for examination. However, because $\geq$ 25 keV HXR emission is caused by mildly relativistic electrons, the expected time-of-flight differences are small, (a few tens of milliseconds), and is close to the time-resolution and sensitivity limit of current HXR detectors. It is therefore not surprising that no positive detection of this effect has been reported up to now. In a recent study of 10 intense flares observed with *HXRBS/SMM*, a systematic delay of HXR pulses at low energies has been identified in 3 flares, using the coincidence with radio bursts and an epoch-folding technique to increase the signal-to-noise ratio (Aschwanden et al. 1995). However, only the advent of high-sensitivity data from *BATSE/CGRO* made a breakthrough possible in the analysis of subsecond time structures. In a preliminary analysis of a structure-rich flare observed by BATSE with 64 ms time resolution, a time delay of 23 ms was reported for the HXR flux in the low-energy channel, but this small effect was not considered to be significant (Machado et al. 1993b). It was concluded that time-of-flight effects are

not present in solar HXR data, or the flare loops are too small to allow time-of-flight measurements. Clearly, a thorough effort with large statistics is needed to investigate this effect. Thus we decided to analyze the largest available high-time resolution dataset from BATSE/CGRO, and to develop an automated structure recognition algorithm that is able to measure energy-dependent time delays by discriminating and correlating fast time structures. We explored also systematic effects in delay measurement techniques and developed a method to estimate systematic errors introduced from background-subtraction methods.

The data analysis and numerical tests on systematic errors are described in §2. We present the statistics on the detected time structures and the results of the energy-delay measurements in §3. Systematic errors and the interpretation of the time delays in terms of time-of-flight differences are discussed in §4. An observational summary and conclusions are given in §5.

2. DATA ANALYSIS

2.1. Observations

We analyze solar flare data observed with the *Burst and Transient Source Experiment (BATSE)* onboard the spacecraft *Compton Gamma Ray Observatory (CGRO). BATSE* consists of 8 *Large Area Detectors (LADs)*, placed at the 8 corners of the spacecraft, each with a sensitive area of 2025 cm^2. The *LAD* detectors are made of NaI scintillation crystals, shielded with plastic scintillation detectors in anticoincidence to reduce the background due to charged particles. Instrumental descriptions of the detectors can be found in Fishman et al. (1989; 1992).

BATSE observed a total of 4360 solar flares during the first 3 years in orbit, from 1991 April 21 to 1994 April 22. These flares were recorded with a time resolution of 1.024 s in 4 energy channels, i.e. 25-50 keV, 50-100 keV, 100-300 keV, and > 300 keV, in the so-called *"background data mode"* (*DISCLA* data type). A higher time resolution of *BATSE* data is available in the *burst trigger mode*. About 15% (659 events) of these solar flares were sufficiently intense to activate the "burst trigger mode". A burst trigger on *BATSE* requires a significant increase (on a threshold nominally set at 5.5 σ) on one of the three time scales: 64 ms, 256 ms, and 1024 ms. The discriminator rates in channels 2 and 3 ($\approx$60-325 keV) are used, and at least two detectors must exceed the threshold for a burst trigger to occur. For this study we used burst trigger data recorded from the *Discriminator Science*

Data (DISCSC) mode, with a time resolution of 64 ms, in the same 4 energy channels as the *DISCLA* count rates, summed over the triggered (2-4) *LADs*. There are also *BATSE* data with a higher resolution of 16 ms (*MER* datatype), but the duration of the 16 ms readout is much shorter per flare ($\approx$ 32 s), making it to a far less complete sample than the *DISCSC* dataset. Also, since the mean duration of the analyzed HXR pulses ($\approx$ 650 ms) is much longer than the used time resolution (of 64 ms), a higher time resolution (of 16 ms for *MER*) would not improve the results. The relative time synchronization of the channel readouts is better than a few microseconds (Fishman, private communication), which is important for energy-dependent time delay measurements.

From the 659 *DISCSC* events (from 1991-1994), identified as solar flares at the *Solar Data Analysis Center (SDAC)* at *NASA/Goddard Space Flight Center (GSFC)*, we analyze a total of 640 events (97%), the remaining 3% are not included in our analysis because of data access problems or corrupted data. There should be no selection effect present in the data, except for the fact that the burst trigger favors the larger (and more intense) flares.

2.2. Detection of time structures

Since the scientific objective of this study is the relative timing of HXR emission at different energies, we have first to define suitable time structures. We concentrate only on the lowest two energy channels of *BATSE*, i.e. 25-50 keV and 50-100 keV, because the count rate at higher energies is always lower and has a poorer signal-to-noise ratio. The timing of a pulse is most accurately defined for short pulses on one hand (considering the variable pulse shapes), but the signal-to-noise ratio improves with the width (w) of the pulse according to $\sqrt{w}$ on the other hand. Thus, there is some optimal range of time scales where the timing of a pulse can be measured with reasonable accuracy. For this study we have chosen a time scale range of $0.3 - 3.0$ s on empirical grounds: Pulses with shorter duration ($\lesssim 0.3$ s) and sufficient significance ($> 5\sigma$) are rare in *DISCSC* solar flare data, while pulses with a longer duration ($\gtrsim 3$ s) often consist of substructures or have an asymmetric pulse shape that introduces an uncertainty in the measurement of the absolute timing. The selected time scale range covers a full decade. We found it not advisable to cover a larger range, because the definition of a time structure becomes problematic when substructures are resolved on finer scales. This is a fundamental problem in the characterization of time structures in solar flares, which apparently contain a hierarchy of time scales from hours down to milliseconds.

Since there is no unique definition of time structures, we develop a criterion that can be objectively applied by a simple numeric algorithm without any a priori assumptions

on the pulse shape. The easiest recognizable feature of a time structure in HXR data is a flux enhancement, characterized by a local maximum (peak) and two adjacent minima (valleys) of the total flux. This simple mathematical definition exploits information on time structures from the "modulated flux" only, while no information can be retrieved from the "unmodulated" (background) flux without a priori knowledge on the convolved time structures.

The detailed procedure of structure detection is accomplished as follows. For definition of the parameters see also Fig. 1. First we apply a low-pass filter with a cutoff of 1.5 Hz to the count rate $C(t)$ (with a time resolution of $\Delta t = 64$ ms), which eliminates high-frequency components with a wavelength of ≤ 0.66 s, or pulse structures with a full width at half maximum (FWHM) of $\lesssim 0.33$ s. From the filtered time profile we identify the local flux maximum $C_P = C(t_P)$ at the peak time t_P of a structure, and define its start (t_1) and end time (t_2) by the times of the adjacent local flux minima. We limit the maximum width w of a time structure to $\lesssim 3$ s on either side. For each structure peaking at time t_P we evaluate a local background $B(t)$ by linearly interpolating the adjacent flux valleys $[B_1 = B(t_1), B_2 = B(t_2)]$ on either side. Each structure is then characterized by the flux enhancement $F(t) = C(t) - B(t)$ above the background $B(t)$. We characterize the width w of the structure by the equivalent width of a rectangular pulse with the same total counts integrated above the linearly interpolated background $B(t)$, i.e.

$$w = \Delta t \sum_{t_i=t_1}^{t_2} \frac{C(t_i) - B(t_i)}{C(t_P) - B(t_P)} = \Delta t \sum_{t_i=t_1}^{t_2} \frac{F(t_i)}{F(t_P)} \; , \tag{1}$$

The values at the peak time t_P are shortly denoted with the index P, i.e. $F_P = F(t = t_P), C_P = C(t = t_P)$, and $B_P = B(t = t_P)$.

We perform a significance test for each structure by requiring an excess of a threshold of $N_\sigma \geq 5\sigma$, using Poisson statistics to estimate the significance level, i.e.

$$N_\sigma = \frac{(C_P - B_P)\, w}{\sqrt{B_P\, w}} = \frac{F_P\, w}{\sqrt{B_P\, w}} \; . \tag{2}$$

This structure detection and 5σ-significance test is applied to each structure in the lower channel. Since we are interested in cross-correlation with structures in the second energy channel, we search for significant structures in identical time windows in the second channel, and accept only those structures for further analysis that pass also a 5σ-significance test in the second channel.

2.3. Time delay measurement

After having identified the time intervals (t_1, t_2) for each significant HXR pulse in each flare, we determine the relative time delay between the two energy channels (E_1, E_2) simply by cross-correlation of the background-subtracted count rates $F(t, E_1) \times F(t, E_2)$ within the time interval $t_1 < t < t_2$ for each pulse. The cross-correlation coefficient $CCC(\tau)$ is then smoothed with a triangular weighting function extending over 5 time bins (with the relative weights 1:2:3:2:1 at $t_{i-2}, t_{i-1}, t_i, t_{i+1}, t_{i+2}$) to filter out data noise (occurring in the case of short or weak pulses with a relatively small number of counts). The energy-dependent delay τ of the HXR pulses is then measured from the time of the maximum in the cross-correlation coefficient function, i.e. $CCC_{max} = CCC(\tau)$, using a second-order interpolation trough the 3 nearest points at the maximum, to overcome the quantization of the finite time resolution Δt. An example of the structure detection and cross-correlation procedure is illustrated in Fig. 2, where the analysis of the first 5 HXR pulses of the flare 1991 June 15 is shown.

There are two conceivable sources of systematic errors in this technique of time delay measurement: (1) the smoothing of the cross-correlation coefficient, and (2) the influence of the linear background. First, the smoothing of the cross-correlation coefficient has no effect on delay measurements for symmetric pulses, or for pulses with widths larger than the triangular weighting function. Since the triangular weighting function (extending over 5 bins) has a FWHM of 3 bins, which is $3\Delta t = 192$ ms, it should not introduce any bias for all pulses analyzed here, which have a minimum duration of $w \gtrsim 0.3$ s according to the time scale restriction. Second, the subtraction of a linear background from a pulse can introduce a substantial shift in the peak time of a pulse, and thus in the relative delay measurement, depending on the steepness of the slope. In the statistical average, we expect that these effect should cancel out, provided that there is a comparable number of cases with positive and negative background slopes. Because we do not have information on the true pulse shape, and thus on the proper background flux, we perform both methods in order to investigate systematic errors introduced by the background subtraction.

2.4. Numerical tests and systematic errors

An obvious test to examine the correctness and accuracy of our numeric code is to generate templates of flare-like time profiles with predefined time delays between pulses at 25 keV and 50 keV, and to compare them with the values found from our numeric code, which performs structure detection and delay measurements in an automated way.

In a preliminary test we generated templates for time profiles by randomly weighted linear combinations of three selected flares, where variable time delays were built in, randomly drawn from a predefined normal distribution. We ran over 1000 random

representations and obtained statistics on some 30,000 pulses. The numeric code was able to reproduce the distribution of time delays close to the parent distribution, but we noticed some significant deviations of their means. In order to isolate this effect we degenerated the delay distribution to a delta-function, i.e. with a mean and a width of zero. For this simulation we found a significant delay of $\tau = 14.3 \pm 0.3$ ms for the mean of the distribution in the case of no background subtraction, and a value of $\tau = 8.9 \pm 0.1$ ms in the case of background subtraction. This indicates some systematic error in the delay measurement, which does not cancel out even in the case of large statistics. Because it is not clear, whether this systematic error was specifically related to the 3 chosen test flares, we decided to employ a larger, more representative flare data set for further testing.

Test 1 (noise-free): We established a representative test dataset of 181 flares by selecting those flares (of the entire data set of 640 flares) that exhibited at least 10 significant HXR pulses (with $> 5\sigma$ in both energy channels). This subset covers only 28% of the flares, but contains about 50% of all analyzed HXR pulses. In a first test we wanted to study systematic errors introduced by the HXR pulse shape and background subtraction method. We mimicked HXR structures with no time delay, with identical pulse shape, and identical noise characteristics by substituting the flux values of the second energy channel with the flux values of the first channel, scaled to the same flux ratio as the original two channels. Naively, a mean delay of zero is expected for this setup. The resulting time delay distributions are shown in Fig. 3 (left hand side). The mean delay is $\tau = 16.2 \pm 0.8$ ms in the case of the unprocessed raw data, while it improves to $\tau = 5.6 \pm 0.1$ ms in the case of background subtraction. Obviously, the method of background subtraction, which relies on the linearly interpolated flux between the adjacent valleys of a pulse, reduces systematic errors in the time delay measurement quite a bit, but not completely. Note also, that the width of the time delay distribution is significantly reduced with the background subtraction method, i.e. from $\sigma_\tau = 43.4$ ms to $\sigma_\tau = 7.2$ ms. In this test setup, the only difference between the two energy channels is a scaling factor, which enters also the ratio of the slopes of the pulse background. Thus, all systematic errors in this test result from asymmetric pulse shapes (in the case of unprocessed raw data) and from the slope of the estimated background (in the case of background subtraction). The fact that we find a significant deviation of the mean delay in this case implies that the asymmetry of the pulse shapes and background slopes do not cancel out with large statistics, but are a fundamental property of the sample of analyzed solar HXR pulses. A systematic error with a positive sign in the offset of the time delay could be produced either if more HXR pulses occur during the risetime of a flare (when the slope of the background is positive) or if the HXR pulses during the risetime are larger (in flux and/or width) than during the decay time of a flare. Note, that this systematic error in the time delay (of 7 ms) is still relatively small

compared with the instrumental resolution (64 ms) or compared with the median duration of the analyzed HXR pulses ($\approx$ 650 ms).

Test 2 (with noise): A more realistic variant of Test 1 is to add Poisson noise to the second energy channel that is independent of the first channel. Thus, we used the same test data as in *Test 1*, and substituted the count rate of the second energy channel by the count rate of the first one, after we scaled it to the proper flux ratio and added random noise with Poisson statistics to the smoothed count rate. Again we ran our automated numeric code to detect significant structures and measured their energy-dependent time delays. The results are shown in Fig. 3 (right hand side). The most prominent difference with regard to *Test 1* is the broadening of the delay distribution, i.e. from $\sigma_\tau = 43.4$ ms to 63.2 ms in the case of the unprocessed raw data (Fig. 3 top), or from $\sigma_\tau = 7.2$ ms to 40.0 ms in the case of the background-subtracted data. This reflects a larger uncertainty in the time delay measurement of an individual pulse due to increased data noise. However, because random noise in the data should cancel out and should not introduce systematic errors, we expect the same means of the two distributions in test 1 and 2. Indeed does the systematic error remain comparable in both cases, in the order of 16-20 ms for the raw data, and 6-9 ms in the case of background-subtracted data. We will use these values for correcting the effectively measured time delays in the real flare data.

3. RESULTS

The almost complete *DISCSC* database with 640 flares analyzed here provides a large representative sample of HXR time structures in the range of 0.3-3.0 s, uniformly recorded with a high time resolution of 64 ms. Based on our structure detection algorithm we found significant ($> 5\sigma$ in both channels) structures in 73% (464 events) of the flares. The automated structure search yielded a total of 5430 HXR time structures, which are called HXR pulses in the following.

First we describe the statistical characteristics of these HXR pulses, especially the distributions of their durations, amplitudes, and rate per flare (§3.1). The results of the energy-dependent time delay measurements are presented in §3.2.

3.1. Statistics of HXR time structures

3.1.1. Pulse widths

The width w or duration of the analyzed HXR pulses, measured by the equivalent width as defined in Eq.1, is shown in Fig. 4. The distribution of the widths can roughly be characterized by an exponential distribution $N(w) \propto exp(-w/w_e)$ in the considered range of $0.3 > w > 3.0$, with an almost identical e-folding time scale for both energy channels, i.e. $w_e = 0.41$ s for the energy range of 25-50 keV, and $w_e = 0.44$ s for 50-100 keV. A characteristic value of the pulse width is the median, i.e. $w_{med} = 650$ ms. A scatterplot of the widths w_{25} versus w_{50} is shown in Fig. 4 (right hand side). The width of the HXR pulses are almost identical in the two energy channels, in the statistical average. A linear relation with slope of unity (Fig. 4, dashed line) and two linear regression fits with exchanged ordinates and abscissae (Fig. 4, solid lines) are shown. The difference in the slopes between the two linear regression fits indicates that there is no significant deviation from unity slope.

3.1.2. Pulse amplitudes

The total HXR count rate at the peak of a pulse, C_P, can be decomposed into a background flux B_P (linearly interpolated between the start and end of the pulse) and a flux enhancement $F_P = C_P - B_P$. The distributions of the total count rate $N(C_P)$ and the pulse count rate $N(F_P)$ are shown in Fig.5 left for both energy ranges. The 50-100 keV count rates can be characterized by a power-law distribution with a slope of ≈ -1.8 over almost the entire observed range. For the lower energy range of 25-50 keV, the distributions show larger deviations from a power-law and have differing slopes.

The pulse fluxes at the two energies are strongly correlated, their relation can be described by the function $F_{50} \propto F_{25}^{1.21}$ (Fig. 5, right hand side). The scatterplot shows a sharp truncation at $F_{50} \approx 250$ cts s^{-1}, which is caused by the 5σ-significance criterion. The scatterplot shows that the high energy flux F_{50} of a pulse is generally smaller than the low energy flux F_{25}, implying that the spectral slope is generally steeper at the peak than at the valley of a pulse. This spectral steepening during a HXR pulse is most pronounced for weak pulses ($F \lesssim 10^4$ cts s^{-1}), and is almost nonexistent for stronger pulses (at $F \approx 10^5$ cts s^{-1}). Because we have no reliable information on the correct background of a pulse, this variation in the slope between peaks and valleys does not necessarily imply a spectral variation over the course of a HXR pulse. It is also interesting to note that this slope variation is negligible for large HXR pulses, where the relative contribution from background subtraction errors is expected to be smallest.

The width and amplitude of the pulses do not show a strong correlation. At low energies (25-50 keV) there is a weak trend that pulses with a larger amplitude have a larger width, but at higher energies (50-100 keV) no trend is discernible between pulse width and

amplitude.

3.1.3. Pulse rate per flare

The number of detected HXR structures per flare should be considered as a lower limit because the detection criterion is restricted by the required minimum significance (of 5σ) in both energy channels. Given this restriction, we detected significant HXR pulses in 73% of the flares recorded with a burst trigger. The distribution of the number N_P of HXR pulses per flare is shown in Fig. 6, reaching up to a maximum of 80 HXR pulses per flare. The distribution can roughly be characterized by an exponential distribution, i.e. $\mathcal{N}(N_P) \propto exp(-N_P/15)$.

3.2. Energy-dependent time delays

The primary goal of our analysis is to quantify the relative timing of HXR pulses between the two energy ranges of 25-50 keV and 50-100 keV, i.e. to determine the distribution of time delays $\tau = t(25keV) - t(50keV)$. The distribution of time delays as measured with the technique described above is shown in Fig. 7, for the unprocessed raw data (Fig. 7 top) and using the described background subtraction method (Fig. 7 bottom). The distribution of time delays measured from the unprocessed raw data can be characterized with a gaussian, with a mean ($\pm$ uncertainty) of $\tau = 30.4 \pm 1.6$ ms and a standard deviation of $\sigma_\tau = 84.8$ ms. The mean time delay is positive, which means that the pulses at the higher energy preceed the pulses at the lower energy for most of the cases. If we restrict our analysis to HXR pulses with a higher significance (of $\mathcal{N}_\sigma > 10$), in order to reduce the effect of data noise in the time delay measurement, the results do not change much, the mean delay is $\tau = 37.5 \pm 2.0$ ms, and the standard deviation is $\sigma_\tau = 77.6$ ms (hatched distribution in Fig. 7 top).

3.2.1. Background subtraction and correction of systematic errors

A subtle issue of the pulse definition is the background subtraction. Since we have no justified model on the pulse shape we pursued both options of cross-correlation, with and without background subtraction. If we subtract an estimated background (linearly interpolated from the flux values at the adjacent valleys on either side of a pulse), the mean time delay reduces by about 10 ms, which corresponds to 30% of the measured delay

time. The distribution of time delays is still gaussian-like (Fig. 7, bottom), with a mean of $\tau = 21.8 \pm 1.5$ ms for HXR pulses with a significance of $N_\sigma > 5$, and $\tau = 26.4 \pm 1.5$ ms for $N_\sigma > 10$, respectively. The reduction of the mean time delay by ≈ 10 ms using the background subtraction method is also consistent with zero-delay test simulations shown in Fig. 3. Therefore, it represents a systematic bias that is inherent to asymmetries in the pulse shapes and background slopes of the analyzed sample.

We correct for this systematic error in the time delay measurement (to first order) by subtracting the bias values found in the test measurements with zero-delay simulations. The relevant values and corrections are listed in Table 1 (for the HXR pulses with $> 10\sigma$ significance). The correction, which differs by ≈ 10 ms whether the background subtraction is applied or not, leads for both correction methods to almost identical results, i.e. 19.7 ms and 19.0 ms for the two methods. This redundancy in the correction methods gives us some confidence that the systematic errors are corrected self-consistently, regardless what type of background subtraction method is applied.

3.2.2. Systematic dependence on pulse parameters

We investigate whether the energy-dependent time delay (τ) has a systematic dependence on other pulse parameters, such as on the significance of a pulse (N_σ), on the pulse width (w), or on the pulse amplitude (F). Scatterplots of the measured time delay as function of these other pulse parameters are shown for the 25 keV pulses in Fig. 8, using the background-subtracted data. In order to find a trend, we perform linear regression fits of the time delay as function of the other parameters (on logarithmic scale). There is almost no dependence of the time delay on the total flux (C) at the peak of a pulse (Fig. 8 bottom right), which largely consists of (apparently) unrelated background flux. The slope of the linear regression fits with other parameters indicates a weak trend that the measured delay increases with the size of a pulse, quantified either in terms of significance, pulse width, or pulse flux. This trend amounts to an increase of 22, 12, or 14 ms in the measured delay, if the significance, the pulse width, or the pulse flux increases by a factor of 10 (in the case of 25 keV pulses). The corresponding values are similar for the 50 keV pulses, i.e. 13, 20, and 6 ms. Despite these weak linear trends, the main result of a positive energy delay remains robust over the entire investigated parameter ranges. We do not correct for these second order effects, since a first-order correction was already applied from the test simulations of systematic errors described above.

The energy delay τ varies also from flare to flare. The mean value τ, the uncertainty of the mean $m_\tau \approx \sigma_\tau / \sqrt{N_P}$, and the standard deviation σ_τ of the delay is shown in Fig. 9 for

flares (181 events) that exhibit more than 10 HXR pulses, using the background-subtracted data. Note that 70% of the flares show a significant positive delay ($\tau - m_\tau > 0$), while only 2% show a significant negative delay ($\tau + m_\tau < 0$).

4. DISCUSSION

This work represents the first systematic study on temporal structures of HXR data of solar flare data with high-time resolution (of 64 ms), with unprecedented instrumental sensitivity (provided by BATSE/CGRO), and large statistics (using all burst trigger data available during three years around the maximum of a solar activity cycle). This unique dataset allows us to study the distribution of time scales (§4.1) and energy-dependent time delays (§4.2). Interpreting the energy-dependent time delays in terms of electron time-of-flight effects (§4.3), we can directly relate the inferred path differences to coronal altitudes of particle acceleration sources (§4.4), employing the thick-target model (§4.5).

4.1. Time scales of HXR time structures

The finding of a continuous distribution of time scales in the investigated range of 0.3-3.0 s rules out the existence of preferred time scales (within this range). The explored range covers only one order of magnitude, and thus, a hierarchy of time scales over larger ranges is not excluded. Elementary time scales of HXR time structures on scales of ≈ 5 s were constituted by DeJager & DeJonge (1978), while a second "fundamental time scale" on the order of ≈ 0.5 s was proclaimed by Machado et al. (1993a; 1993b), based on the most frequent structures seen in some flares recorded by *BATSE/CGRO*. Although we did not explore a sufficiently large time range that extends beyond these two so-called "elementary time scales", we do not see an indication of a preferred time scale or a bimodal distribution in the range of 0.3-3.0 s. The peak at $\approx 0.4 - 0.5$ s in the time scale distribution (shown in Fig. 4) is consistent with the rollover caused by the artificial FFT cutoff and the 5σ-significance criterion in our detection procedure. The continuous distribution of time scales with an exponential behavior (in the range of 0.3-3.0 s) is consistent with a random process governed by Poisson statistics.

A more important implication of our statistics of HXR time scales is the fact that the average duration of a HXR pulse was found to be identical at different energies, say at 25 keV and at 50 keV. Because the collisional energy loss time varies with kinetic energy ε as $\varepsilon^{3/2}$, the equality of time scales at different energies cannot be explained either by

collision or by trapping effects. Consequently, the underlying time scale seems rather to be the duration of a basic acceleration or electron injection pulse. In recent studies, the duration of HXR pulses was found to correlate with the duration of coincident radio type III bursts on time scales of 0.2-1.0 s, implying that both the radio and HXR signatures are controlled by common electron acceleration/injection pulses (Aschwanden, Benz & Schwartz 1993; Aschwanden et al. 1995). From these two arguments, i.e. the energy-invariant time scale and the correlated duration of HXR pulses and type III bursts, we conclude that the subsecond HXR pulses are of nonthermal origin associated with the acceleration and injection of electron beams. Although thermal HXR signatures often occur concomitantly with nonthermal emission in the $\geq$ 25 keV energy range, the thermal component is more likely to be part of the smooth HXR continuum, which has been filtered out in the background-subtracted analysis of subsecond HXR pulses here.

4.2. Systematic errors in time delay measurements

The principal goal of this study is the measurement of time delays between HXR time structures at different energies. This task can be done with different techniques, and the answer strongly depends on the systematic errors inherent to each technique. Thus we like to discuss in this section some systematic effects that can be corrected for and may lead to a self-consistent answer independent of the applied technique.

First of all, the most crucial part is the definition of a time structure. An arbitrary time segment of HXR flux may consist of a hierarchy of structures that can have different time delays at the same time. Depending how good a filter technique can separate the different hierarchical time structures, the time delay of each component can be retrieved independently, although they may occur simultaneously. For instance, while time-of-flight differences of injected electrons may cause a positive delay for the HXR emission of low-energy electrons, there may be at the same time HXR emission produced by precipitating electrons that leak out of a trap, which probably exhibit a negative delay (for low-energy electrons), because their collisional time scale is increasing with energy. These two effects can only be disentangled if they have different characteristic time scales. The measured time delay depends then strongly on the selected time scale. In our study we focused on fast time structures mostly on subsecond time scale, which are more likely to be associated with electron beam injections than with emission from trapped particles. The structure detection algorithm allowed us to select a specific range of time scales and to perform the time delay measurements for those pulses independently from other delays present in the same data (at other time scales). This cannot be achieved if the whole (unfiltered) HXR time profile is cross-correlated (between two energy bands). In the latter

case, the resulting delay would be dominated from those time structures which contain the largest fluxes.

Another systematic bias in time delay measurements via cross-correlation techniques is the subtraction of a background. An additive constant in the background should not affect the peak time of the cross-correlation coefficient (from which we measure the time delay). However, a background with some slope shifts the centroid of a structure. If a linear background is added with the same slope to two structures (at different energies), the centroid is shifted by the same amount in both structures, and the peak time of the cross-correlation remains invariant, because it is only sensitive to the relative position of the centroids. However, the slope of the background flux of HXR pulses at 25 keV and 50 keV is generally not identical, but is rather expected to be proportional to the flux ratio of the two channels, given the overall proportionality that generally occurs between the two energy channels (see Fig. 5). A scheme for correcting this systematic bias is sketched in Fig.10. If the overall flux ratio between the 50 keV and 25 keV flux is q, a cross-correlation of the total flux C_{25} with an identical pulse qC_{25} scaled to the flux of the second channel would already introduce an artificial delay τ_{corr} because of the different slopes, although the pulses are simultaneous. The correct delay τ between the 25 keV and 50 keV pulse can be measured from cross-correlating qC_{25} with C_{50}, because they have an identical slope, regardless what the level of the true background flux is. This is illustrated for 3 cases in Fig.10, where the true background level amounts to 100%, to 80%, or 0% of the lower envelope to the pulse. The cross-correlation between qC_{25} and C_{50} yields an invariant measure of the delay, independent of the estimated background, while the direct correlation of C_{25} with C_{50}, lets call it τ_{raw}, yields an erroneous result if the background slopes are not identical. Because the difference in the background slope is the same for the two correlations $C_{25} \times qC_{25}$ and $C_{25} \times C_{50}$, the corrected value of the energy delay τ can be derived from their difference, i.e.

$$\tau = \tau_{raw} - \tau_{corr} \tag{3}$$

An empirical proof for the correctness of this model is given in Table 1, where Eq.3 was applied, leading to an invariant, corrected value of $\approx$ 19 ms for the energy delay, regardless whether the unprocessed raw data were used (Fig. 9 right hand side), or if a linear background was subtracted (Fig. 9 left hand side). The only assumption made in this correction procedure is that the (unknown) background has a slope ratio proportional to the flux ratio of the two energy channels.

4.3. Time-of-flight effects

The finding of a significant, positive time delay of HXR pulses at low energies (25-50 keV) with respect to higher energies (50-100 keV) can be interpreted in terms of a propagation time difference, assuming that the HXR-emitting electrons in both energy bands have about the same propagation path. We are not aware of other models that could account for a positive time lag for low-energy electrons. Alternative models that deal with energy-dependent time delays are the trap-plus-precipitation model (Melrose & Brown 1976), or the second-step acceleration model (Bai & Ramaty 1979). But because both of them predict an opposite sign in the energy-dependent delay, we do not consider them further.

We consider a simple flare scenario in which electrons of all energies are injected simultaneously in a coronal height h_0 and precipitate along the magnetic field lines of a flare loop down to a chromospheric height h_X where they produce HXR by thick-target bremsstrahlung. If we assume the injection site to be placed near the top of a flare loop, the time-of-flight difference τ between two electrons with different velocities $\beta_1 = v_1/c$ and $\beta_2 = v_2/c$ is

$$\tau = \frac{\pi}{2}\frac{(h_0 - h_X)}{c\cos\alpha}\left(\frac{1}{\beta_1} - \frac{1}{\beta_2}\right) \tag{4}$$

with α being the pitch angle. To produce a HXR photon with energy E_i, electrons with a kinetic energy ε in the range of $1 < \varepsilon/E_i \lesssim 3$ are required, based on the Bethe-Heitler cross-section for bremsstrahlung, assuming a power-law spectrum with slope $\gamma \gtrsim 3$ for the injection spectrum (Kosugi, Dennis & Kai 1988). Thus, we estimate the kinetic energy ε of the electrons that produce HXR photons with energies $E > E_i$ by the approximation $\varepsilon_i \approx 2E_i$. We obtain the speed β_i from the relativistic relation $E_{kin} = m_e c^2(\gamma - 1)$ (with γ the Lorentz factor), i.e.

$$\beta_i(E_i) = \sqrt{1 - \left(1 + \frac{2E_i}{511\ keV}\right)^{-2}}. \tag{5}$$

Averaging a typical photon spectrum (with slope E^{-4}) over the *BATSE* detector response function, the representative photon energy is $E_1 = 40$ keV in the 25-50 keV channel, and $E_2 = 77$ keV in the 50-100 keV channel. The relevant electron speeds are $\beta_1(E_1$=40 keV)=0.50 and $\beta_2(E_2$=77 keV)=0.64, yielding a factor of $(1/\beta_1 - 1/\beta_2) = 0.44$ in Eq. 4. This factor, which depends on the assumed slope γ of the electron injection spectrum, would change by $\pm 17\%$ if the ratio ε/E is changed by $\pm 50\%$. Assuming a pitch angle of $\alpha = 0$, the height difference $H = (h_0 - h_X)$ inferred from the measured average energy delay of $\tau = 19.4$ ms is then $H = 8400$ km, according to Eq.4. This is a plausible height for flare loops.

4.4. Altitude range of electron injection

From the previous section we inferred the average height of the electron injection site to $H = 8400$ km above the chromospheric thick-target site h_X. The measured distribution of energy time delays is strongly broadened by data noise and methodical uncertainties. In order to estimate the true width σ_τ of the distribution of time delays, we have to deconvolve the measured distribution (with a width of σ_{raw}) with the point spread function of the measurement noise (with a width σ_{noise}). If we assume gaussians for all three distributions, the width of the deconvolved time delay distribution is roughly

$$\sigma_\tau^2 \approx \sigma_{raw}^2 - \sigma_{noise}^2 \tag{6}$$

We estimate the width of the measurement noise from *Test 2*, which is $\sigma_{noise} = 34.4$ ms (see Fig.3, background-subtracted HXR pulses with $N_\sigma > 10$). Comparing with the measured width of $\sigma_{raw} = 50.6$ ms for the corresponding sample of real data (see Fig. 7), we infer a width of $\sigma_\tau = \sqrt{50.6^2 - 34.4^2} = 37.1$ ms for the deconvolved time delay distribution. Translating this value ($\tau \pm \sigma_\tau = 19.4 \pm 37.1$ ms) into an altitude range, we obtain $H \pm \sigma_H = 6300 \pm 16,000$ km. This corresponds to an average footpoint separation of $L = 2H = 24" \pm 46"$, which is a characteristic size of flare loops, as observed in HXR double footpoint sources with *Yohkoh/HXT* (Sakao 1994).

4.5. Implications for thick-target flare models

The finding of a systematic energy-delay for low-energy electrons is an expected result in the thick-target model (Emslie 1983). However, because the effect is relatively small, requiring large statistics and a high signal-to-noise ratio to reduce systematic errors, it could not be reliably determined before the advent of *BATSE/CGRO* data. The measured effect (of ≈ 19 ms) is still below the resolution (of 64 ms) of this dataset, and amounts to only 3% of the typical HXR pulse width (of 650 ms). The establishment of a significant time delay between 25 keV and 50 keV HXR-emitting electrons, which matches the value expected for a time-of-flight difference of simultaneously injected electrons, can be considered as the first direct kinematic proof of the thick-target model.

The smallness of the inferred propagation delay has an important implication on the expected temporal variation of the spectral slope of the HXR spectrum. If electron injection pulses with a duration of $\lesssim 20$ ms would occur, a hard-to-soft evolution would be expected due to the time-of-flight differences. However, for any pulse with a duration

$\gtrsim$ 20 ms, the velocity dispersion due to time-of-flight differences is convolved with the electron injection profile, and the observed spectral variation reflects only the variation of the electron injection spectrum. It is therefore not surprising, that no short-term spectral changes have been observed during subsecond pulses (Machado et al. 1993a; 1993b), except for extremely short HXR pulses, e.g. for a 200-ms spike (Kiplinger et al. 1984).

Another consequence of the inferred time-of-flight distances is a constraint for an upper limit of the electron density in flare loops. If the electron time-of-flight would be shorter than the collision time, they would be stopped before they reach the chromosphere and HXR emission from the lower-energy electrons (which are stopped first) would preceed the thick-target HXR emission from the higher-energy electrons, which is not consistent with our finding. The upper limit of the electron density can be found from the electron collision time, assuming an optically thin plasma for HXR, i.e.

$$n_e[cm^{-3}] \leq \frac{T_e[eV]^{3/2}}{2.91 \cdot 10^{-6}\ \tau_c[s]\ ln\Lambda} \ . \qquad (7)$$

For $T_e > 50$ keV electrons (that produce $\gtrsim 25$ keV HXR emission) and a collision time larger than the inferred time-of-flight ($\tau_c \geq \tau = 19$ ms), with a Coulomb logarithm of $ln\Lambda \approx 25$, we find an upper limit of $n_e \leq 8 \cdot 10^{12}$ cm^{-3}. This upper limit is consistent with typical flare densities, which are found from a few times 10^{10} cm^{-3} to several times 10^{12} cm^{-3} (Doschek 1990).

5. 5. SUMMARY AND CONCLUSIONS

1. We analyzed time structures on time scales of 0.3-3.0 s in 640 solar flares, using high-time resolution (64 ms) data from the burst trigger mode (*DISCSC*) of *BATSE/CGRO*. With an automated structure detection algorithm we identified 5430 HXR pulses with a significance of $> 5\sigma$ in both the 25-50 keV and the 50-100 keV energy channel.

2. The HXR pulses were found to have an almost identical duration (w) at 25 keV and 50 keV, and they have a continuous distribution in the analyzed range of 0.3-3.0 s that can be described with an exponential distribution $N(w) \propto exp(-w/0.4s)$. The constancy of the pulse duration at different energies indicates that the pulse duration is determined by the electron injection function rather than by transport effects.

3. The peak flux F of the HXR pulses can be described with a power-law distribution of $N(F_{50}) \propto F_{50}^{-1.8}$ at 50 keV. This size distribution of HXR flare substructures is

basically identical with the size distribution of HXR flares (Crosby, Aschwanden & Dennis 1993). The pulse fluxes in the two energy ranges are strongly correlated, i.e. $F_{50} \propto F_{25}{}^{1.2}$.

4. The number of pulses N_P per flare can be roughly characterized by $N(N_P) \propto exp(-N_P/15)$, in the range of $N_P < 80$. This distribution is similar to the distribution found for the number of radio type III bursts per flare, i.e. $N(N_{III}) \propto exp(-N_{III}/10.5)$, in the range of $N_P < 60$ (Aschwanden, Benz, & Montello, 1994).

5. The HXR pulses were found to show a significant, positive delay τ between the 25-50 keV and 50-100 keV energy range. This delay has an average of 19.4 ± 1.3 ms, after it was corrected for a systematic bias in the subtraction of the background slope. The standard deviation is estimated to $\sigma_\tau \approx 37$ ms, after deconvolution of broadening effects by data noise and methodical uncertainties. We found that cross-correlation delay measurements are subject to systematic errors due to the slope of the estimated background, which can be self-consistently corrected if the background slope is proportional to the flux ratio of the two energy channels.

6. We interpret this energy delay in terms of electron time-of-flight differences. Assuming particle acceleration and injection near the top of flare loops, and HXR emission near the chromosphere, we infer a height distribution (with a mean and standard deviation) of $H \pm \sigma_H = 6300 \pm 16,000$ km for flare loops. The observational evidence of a systematic time delay of the low energy electrons, that matches the expected electron time-of-flight difference in a typical flare loop, can be considered as the first kinematic proof of the thick-target model.

7. The smallness of the electron time-of-flight differences, which corresponds to a fraction of $\approx 3\%$ of the average HXR pulse width, produces no (hard-soft) variations of the spectral slope, unless the injection pulse is as short as ≈ 20 ms. No rapidly-varying spectral variations are therefore expected during most of the flares.

8. Comparing the electron collision time with the inferred times-of-flight we infer an upper limit of $n_e \leq 8 \cdot 10^{12}$ cm^{-3} for electron densities in flare loops. This is consistent with upper limits found from soft X-ray flare observations (with $n_e \lesssim$ a few times 10^{12} cm^{-3} (Doschek 1990).

This research has made use of data obtained through the Compton Observatory Science Support Center GOF account, provided by the NASA/Goddard Space Flight Center. We

thank the *BATSE* P.I. G.Fishman, the *BATSE* team at MSFC, T.McGlynn, W.Paciesas, R.Wilson, C.Meegan, the CGRO science support center *(GROSSC)*, and the *SDAC* at *GSFC*, namely Eric Carzon, for access and archival services of *BATSE/DISCSC* data. The work of M.J.A. and D.M.A. was partially supported at GSFC and UMd by NASA grants NAS5-30442, NAGW-3456, NAG5-2352, and R.A.S. was supported by CGRO grant NAS5-32584.

	Measured delay [ms]	Systematic error [ms]	Corrected delay [ms]
Raw data	37.5±2.0	17.8±1.2	19.7±2.3
Background-subtracted	26.4±1.5	7.4±0.2	19.0±1.5
Average			19.4±1.3

Table 1: Correction of energy-delay measurements (for HXR pulses with $N_\sigma > 10$)

REFERENCES

Aschwanden,M.J., Benz,A.O. and Schwartz,R.A. 1993, ApJ, 417, 790

Aschwanden,M.J., Benz,A.O., and Montello,M.L. 1994, ApJ, 431, 432

Aschwanden,M.J., Montello,M., Dennis,B.R. and Benz,A.O. 1995, *Correlated Sequences of Hard X-Ray and Type III Bursts during Solar Flares*, ApJ, 440, February 10 issue, in press

Bai,T. and Ramaty,R. 1979, ApJ, 227, 1072

Crosby,N.B., Aschwanden,M.J. and Dennis,B.R. 1993, Sol.Phys., 143, 275

DeJager,C. and DeJonge,G. 1978, Sol.Phys., 58, 127

Doschek,G.A. 1990, ApJ.Suppl.Ser., 73, 117

Emslie,A.G. 1983, ApJ 271, 367

Fishman,G.J. et al. 1989, "The Burst and Transient Source Experiment (BATSE) - Scientific Objectives and Capabilities", *GRO Science Workshop*, GSFC.

Fishman,G.J., Meegan,C.A., Wilson,R.B., Paciesas,W.S. and Pendleton,G.N. 1992, "The Compton Observatory Science Workshop", NASA CP 3137, p.26

Kiplinger,A.L., Dennis,B.R., Frost,K.J., and Orwig,L.E. 1984, ApJ, 287, L105

Kosugi,T., Dennis,B.R., and Kai,K. 1988, ApJ, 324, 1118

Machado,M.E., Ong,K.K., Emslie,A.G., Fishman,G.J., Meegan,C., Wilson,R., and Paciesas,W.S. 1993a, Adv.Space Res. 13/9, 175

Machado,M.E., Emslie,A.G., Ong,K.K., Fishman,G.J., and Paciesas,W.S. 1993b, *Fundamental temporal structures in solar hard X-ray bursts*, ApJ, Lett., submitted

Melrose,D.B. and Brown,J.C. 1976, MNRAS, 176, 15

Sakao,T. 1994, PhD. Thesis, National Astronomical Observatory Mitaka, Tokyo/Japan, *Characteristics of Solar Flare Hard X-Ray Sources as Revealed with the Hard X-Ray Telescope aboard the Yohkoh Satellite.*

Vilmer,N., Kane,S.R., and Trottet,G. 1982, A&A, 108, 306

This manuscript was prepared with the AAS LaTeX macros v3.0.

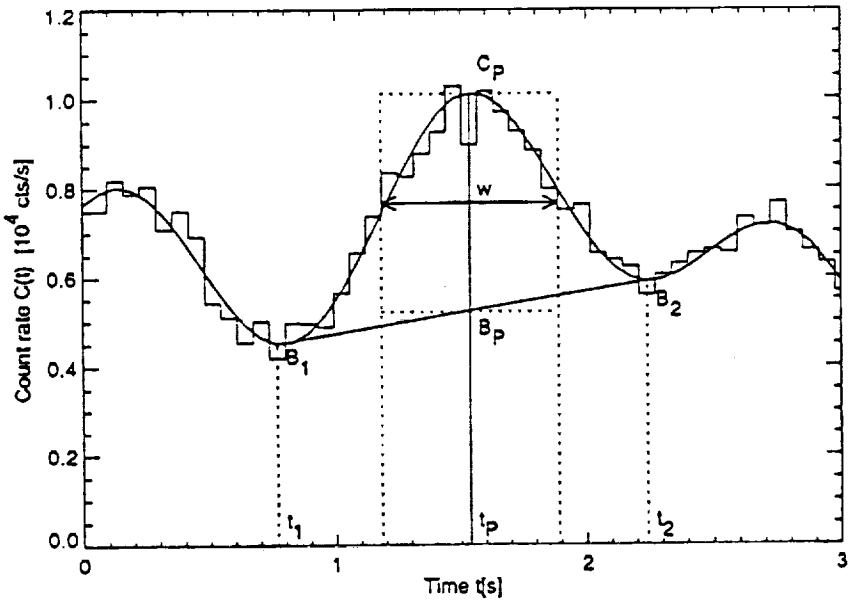

Figure 1 : (Aschwanden, Schwartz, & Alt, 1994)

Fig. 1.— Parameter definition of a HXR pulse: A pulse structure is defined by a local maximum (with peak at time t_P) and two adjacent minima (valleys at times t_1 and t_2) of the (FFT-filtered) count rate (smooth curve). The raw data (histogrammed) are binned with the original time resolution of 64 ms. A local background $B(t)$ of the structure is defined by linear interpolation between the valleys $B_1 = B(t_1)$ and $B_2 = B(t_2)$. The peak count rate $C_P = C_P(t_P)$ and background $B_P = B(t_P)$ are measured at the peak time t_P. The (equivalent) width w of the structure (marked with a double arrow) is determined from the integrated counts $C(t) - B(t)$ (above the linear background) divided by the peak count rate $C_P - B_P$ (see Eq.1).

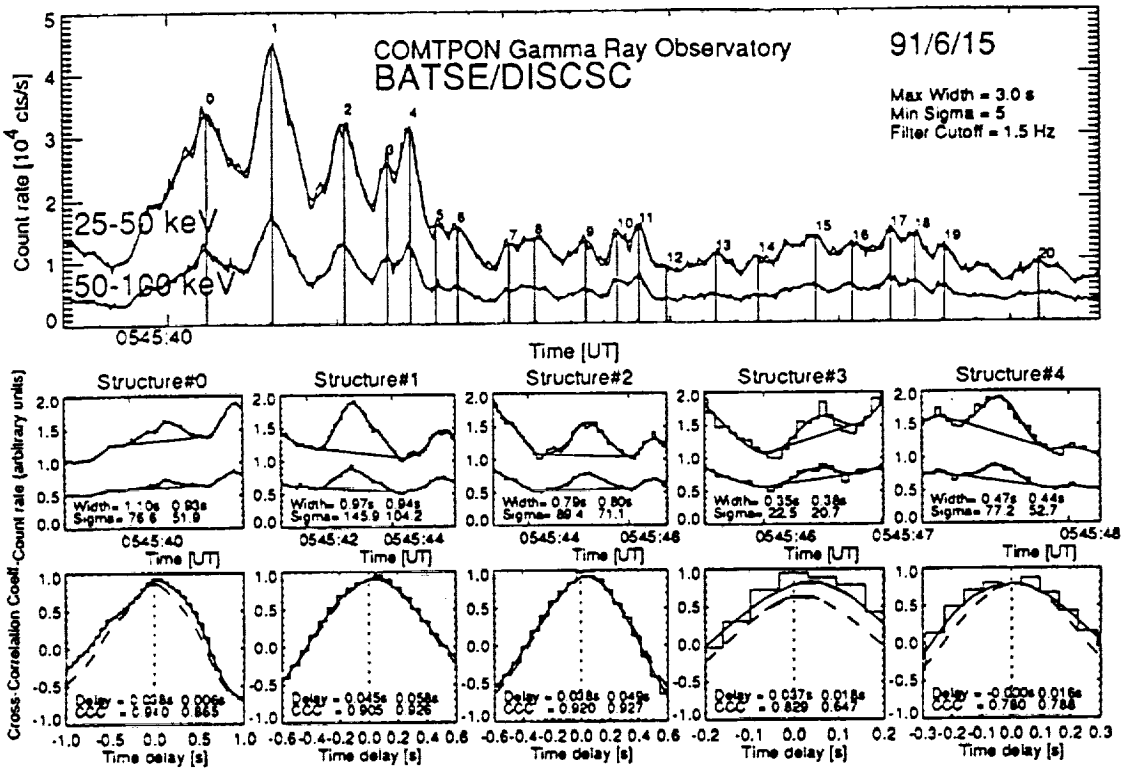

Figure 2 : (Aschwanden, Schwartz, & Alt, 1994)

Fig. 2.— Example of an analyzed flare (91/6/15) using BATSE/DISCSC data with 64 ms time resolution. The count rate of the two lower energy channels 25-50 KeV and 50-100 keV are shown in the upper frame, together with the overlayed lowpass-filtered time profiles (smooth curves) used for structure detection. The numbers #0-20 refer to structures identified with a 5σ- significance in both channels. The first 5 structures #0-4 are shown in detail in the middle row, with the filtered count rate and linearly interpolated background indicated. The equivalent widths w and significance levels N_σ of these structures are indicated for both energy channels inside the panels in the middle row (left for 25 keV, right for 50 keV). The cross-correlation of the count rates of the two energies is shown in the bottom row, for the raw data (histogrammed), and after subtraction of the linearly interpolated background (dashed). The time delay is determined from the maximum of the (smoothed) cross-correlation coefficient, using a second-order interpolation near the maximum. The numeric values of the delay τ and the maximum cross-correlation coefficient (CCC) are also indicated in the bottom panels (for the raw data on the left side, and for the background-subtracted data on the right side). Note that all 5 structures show a positive delay $\tau = t(25keV) - t(50keV)$, regardless of the background-subtraction method.

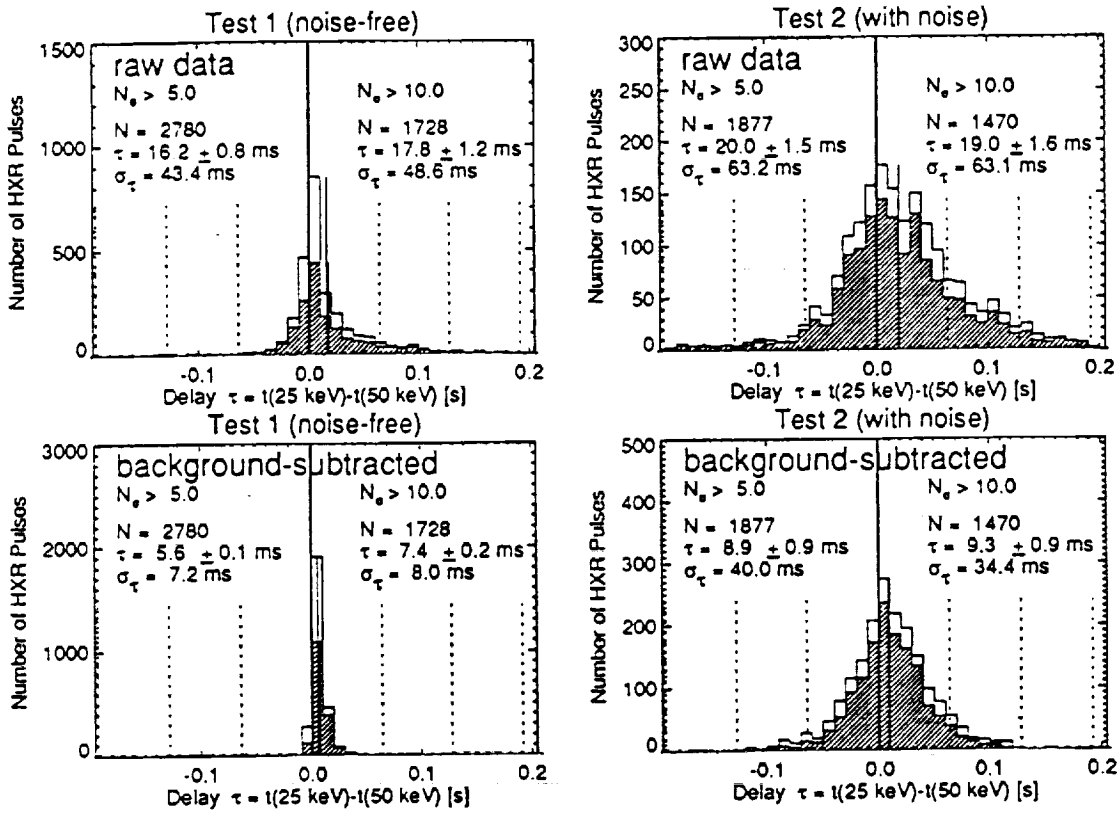

Figure 3 : (Aschwanden, Schwartz & Alt 1994)

Fig. 3.— Test runs of time delay measurements with real flare data in the 25 keV energy channel and (undelayed) artificial data in the 50 keV energy channel. The artificial data are noise-free in Test 1 (left hand side), and contain Poission noise statistics in Test 2 (right hand side). The top panels represent pulse cross-correlations using the raw data, while in the lower panels a background subtraction is applied. Statistics are tabulated for two significance thresholds ($N_\sigma > 5, 10$), including the size of the sample (N), the statistical mean (τ) with uncertainty, and the standard deviation σ_τ of the distribution of time delays. The distributions for $N_\sigma > 10$ are hatched. The dashed lines indicate multiples of the time resolution (of 64 ms). The time bins are 10 ms.

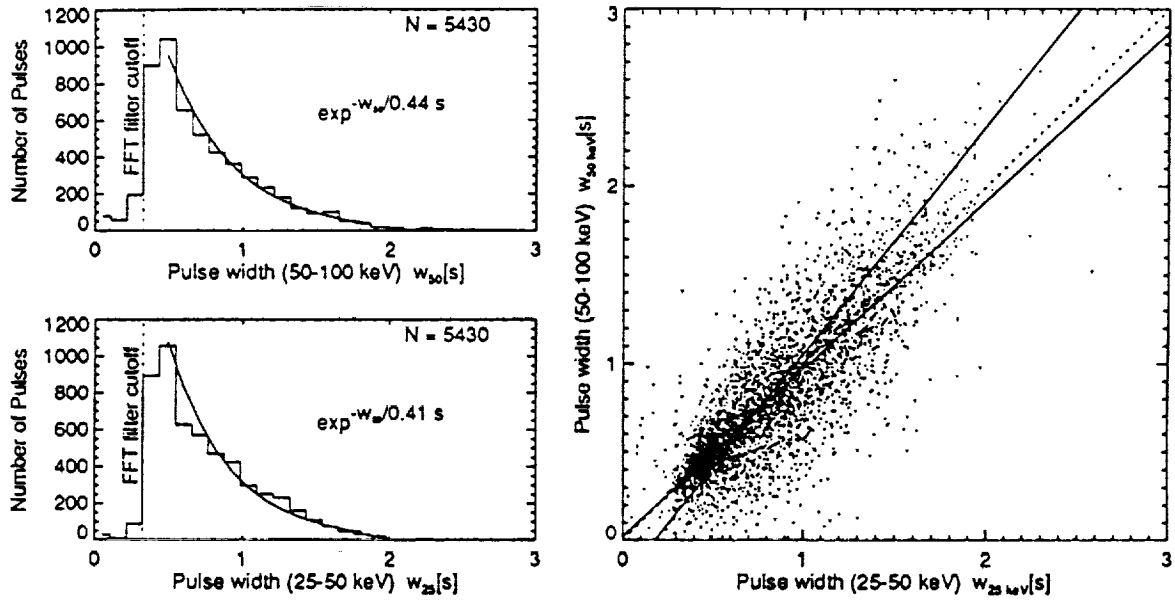

Figure 4 : Aschwanden, Schwartz & Alt (1994)

Fig. 4.— Time scales (FWHM) of hard X-ray pulses in the range of 0.3-3.0 s, in the 25-50 keV range (bottom left), and in the 50-100 keV range (top left). The cutoff of detected time scales at $\lesssim 0.3$ s is caused by the Fourier (FFT) filter of the time series. A scatterplot of the FWHM's w between the two energy channels is shown as scatterplot (right hand side). The time scales in the two energy ranges are roughly equal.

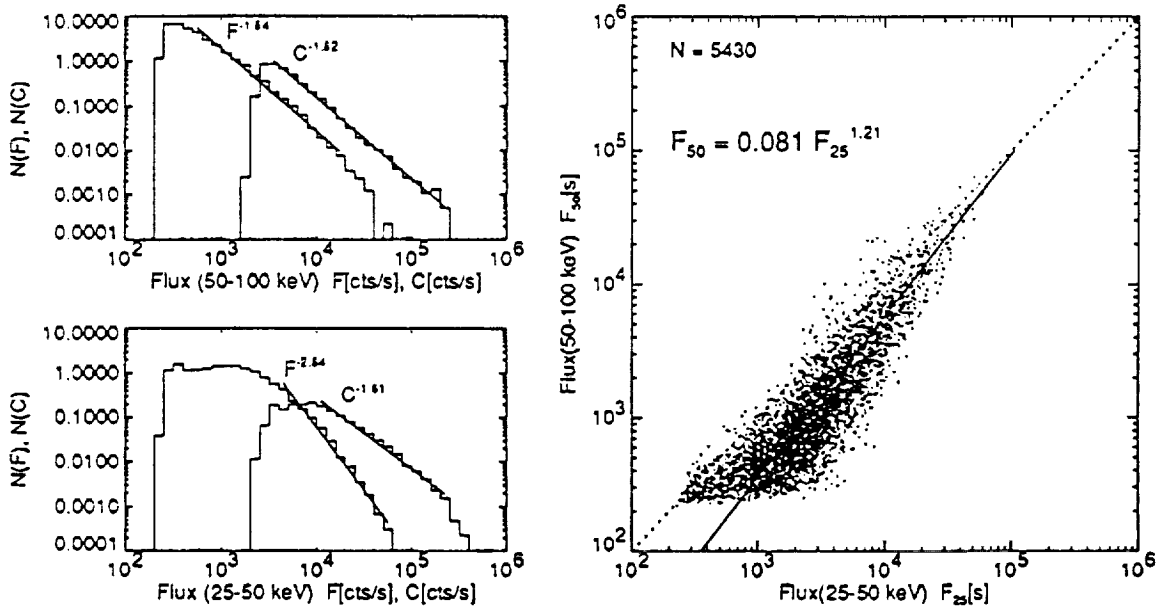

Figure 5 : Aschwanden, Schwartz & Alt (1994)

Fig. 5.— Distributions and scatterplot of HXR fluxes (in counts/s) at 25-50 keV and 50-100 keV. The background-subtracted pulse fluxes are denoted with F, while the total fluxes (including the background flux) are denoted with C.

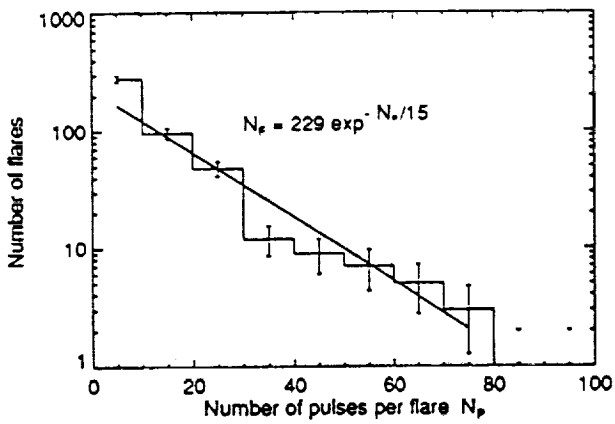

Figure 6 : Aschwanden, Schwartz & Alt (1994)

Fig. 6.— Distribution of the number of detected ($> 5\sigma$) HXR structures per flare.

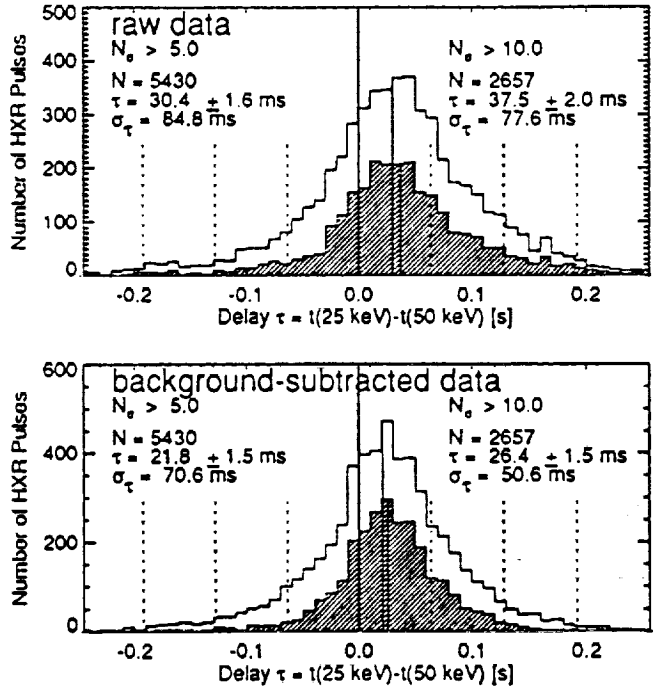

Figure 7 : (Aschwanden, Schwartz & Alt 1994)

Fig. 7.— Distribution of measured time delays $\tau = t(25keV) - t(50keV)$, without background subtraction (top) and using a background subtraction method (bottom). The white histogram includes the statistics of ($> 5\sigma$) structures, while the hatched histogram includes the ($> 10\sigma$) structures.

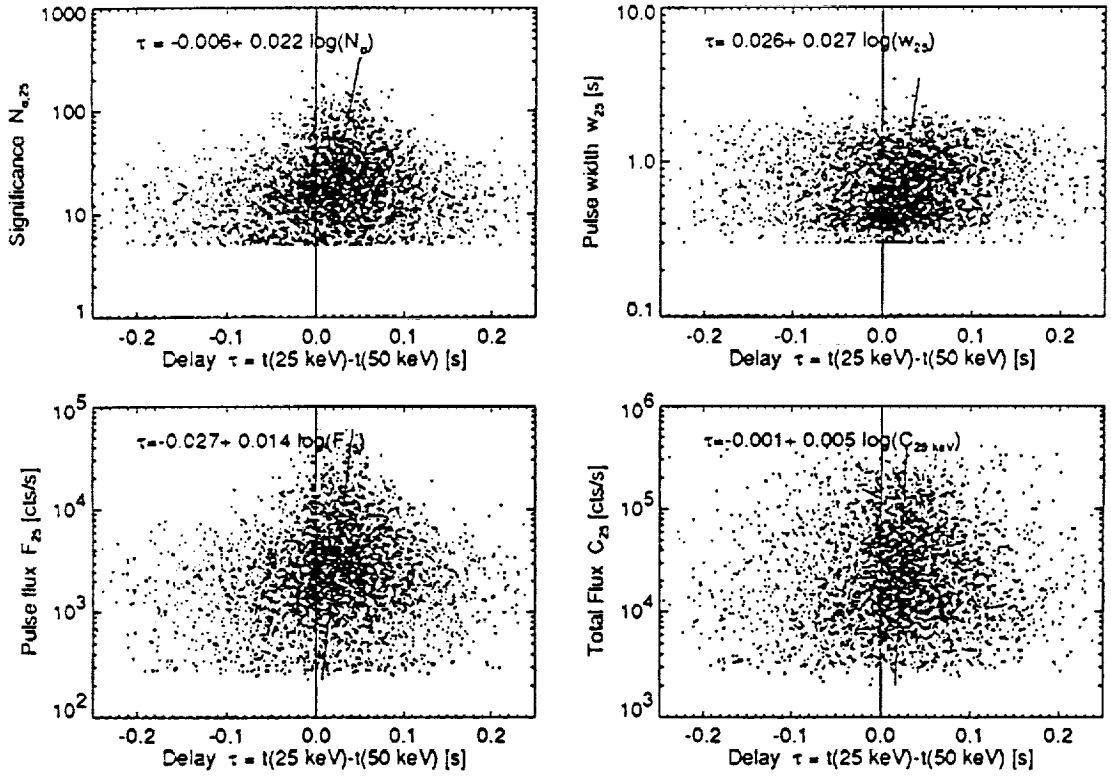

Figure 8 : (Aschwanden, Schwartz & Alt 1994)

Fig. 8.— Scatterplots and linear regression fits of time delay τ versus the following 4 pulse parameters: the significance (N_σ), the pulse width (w), the pulse flux (F_{25keV}), and the total flux (C_{25keV}) at the peak time of the pulse. Note that the time delay τ was used as dependent parameter in the linear regression fits, which has a slope almost orthogonal to the cutoffs produced by the 5σ-significance threshold.

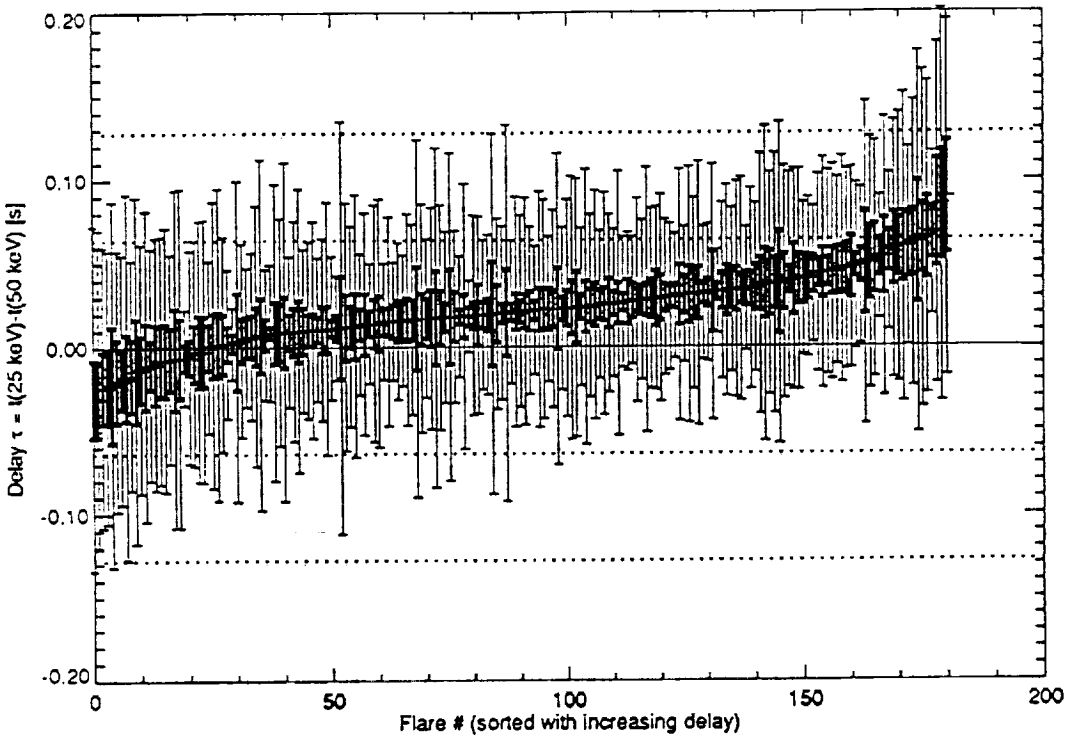

Figure 9 : Aschwanden, Schwartz & Alt (1994)

Fig. 9.— Time delay of HXR pulses at 25-50 keV with respect to 50-100 keV in 181 flares observed with *BATSE/CGRO* that have $N_P \geq 10$ significant ($N_\sigma > 5$) pulses. The mean, error of the mean (thick error bars), and the standard deviation (thin error bars) are indicated for the delays averaged per flare, and sorted with increasing order of the mean. The dashed lines indicate multiples of the time resolution (64 ms). Note that most of the flares have a significant positive delay, while almost none have a significant negative delay.

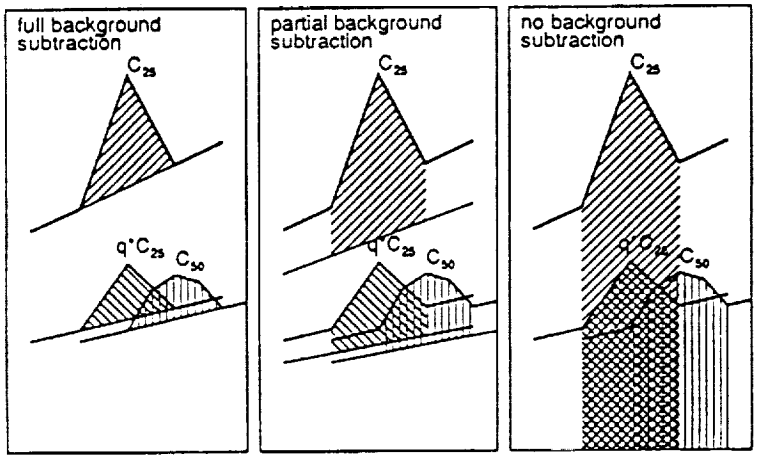

Figure 10 : (Aschwanden, Schwartz, & Alt, 1994)

Fig. 10.— Scheme of background-slope correction in cross-correlation delay measurments, illustrated for 3 cases with 100% (full), 80% (partial), and 0% (no) background subtraction (see text in §4.2).

REPORT DOCUMENTATION PAGE

Form Approved
OMB No. 0704-0188

1. AGENCY USE ONLY *(Leave blank)*	2. REPORT DATE	3. REPORT TYPE AND DATES COVERED
	December 1994	Contractor Report

4. TITLE AND SUBTITLE

Studying the Thermal/Non-Thermal Crossover in Solar Flares

5. FUNDING NUMBERS

Code 668
NAS5-32584
IHK-341-03

6. AUTHOR(S)

R. A. Schwartz

7. PERFORMING ORGANIZATION NAME(S) AND ADDRESS(ES)

Hughes STX Corporation
4400 Forbes Boulevard
Lanham, MD 20706

8. PERFORMING ORGANIZATION REPORT NUMBER

9. SPONSORING/MONITORING AGENCY NAME(S) AND ADDRESS(ES)

NASA Aeronautics and Space Administration
Washington, D.C. 20546-0001

10. SPONSORING/MONITORING AGENCY REPORT NUMBER

CR-189436

11. SUPPLEMENTARY NOTES

Technical Monitor: J. Norris, Code 668

12a. DISTRIBUTION/AVAILABILITY STATEMENT

Unclassified-Unlimited
Subject Category: 89
Report available from the NASA Center for AeroSpace Information,
800 Elkridge Landing Road, Linthicum Heights, MD 21090; (301) 621-0390.

12b. DISTRIBUTION CODE

13. ABSTRACT *(Maximum 200 words)*

This report describes the worked performed under contract NAS5-32584 during the time period covered by Phase 3 of the CCGRO Guest Investigator Program under NRA-92-OSSA-17 from 1 November 1993 through 1 November 1994. We have made spectral observations of the hard x-ray and gamma-ray bremsstrahlung emissions from solar flares u sing BATSE on CGRO. These measurements of th eir spectrum and time profile provided valuable information on the fundamental flare processes of energy release, particle acceleration, and energy transport. Our scientific objective was to study both the thermal and non-thermal sources of solar flare hard x-ray and gamma-ray emission.

14. SUBJECT TERMS

Sun: Corona, Flares, X-ray Radiation, Particle accleration

15. NUMBER OF PAGES

34

16. PRICE CODE

17. SECURITY CLASSIFICATION OF REPORT	18. SECURITY CLASSIFICATION OF THIS PAGE	19. SECURITY CLASSIFICATION OF ABSTRACT	20. LIMITATION OF ABSTRACT
Unclassified	Unclassified	Unclassified	Unlimited